10904 *Biochemistry* **2003,** *42,* 10904−10914

Structure of Avian AICAR Transformylase with a Multisubstrate Adduct Inhibitor β-DADF Identifies the Folate Binding Site[†,‡]

Dennis W. Wolan,[§] Samantha E. Greasley,[§,||] Mark J. Wall,[⊥,@] Stephen J. Benkovic,[⊥] and Ian A. Wilson*[,§]

Department of Molecular Biology and The Skaggs Institute for Chemical Biology, The Scripps Research Institute, 10550 North Torrey Pines Road, La Jolla, California 92037, and Department of Chemistry, Pennsylvania State University, State College, Pennsylvania 16827

ABSTRACT: The penultimate catalytic step of the purine de novo synthesis pathway is the conversion of aminoimidazole-4-carboxamide ribonucleotide (AICAR) to 5-formyl-AICAR that requires the cofactor N_{10}-formyl-tetrahydrofolate as the formyl donor. This reaction is catalyzed by the AICAR transformylase domain of the bifunctional enzyme AICAR transformylase/inosine monophosphate cyclohydrolase (ATIC). Identification of the location of the AICAR transformylase active site was previously elucidated from the crystal structure of the avian ATIC with bound substrate AICAR; however, due to the absence of any bound folate, the folate binding region of the active site could not be identified. Here, we have determined the homodimeric crystal structure of avian ATIC in complex with the ATIC-specific multisubstrate adduct inhibitor β-DADF to 2.5 Å resolution. β-DADF encompasses both the AICAR and folate moieties into a single covalently linked entity, thereby allowing for the characterization of the folate binding pocket of the AICAR transformylase active site. β-DADF is intimately bound at the dimer interface of the transformylase domains with the majority of AICAR moiety interactions occurring within one subunit, whereas the primary interactions to the folate occur with the opposing subunit. The crystal structure suggests that a buried Lys^{267} is transiently protonated during formyl transfer allowing for the stabilization of the oxyanion transition state and subsequent protonation of N10 on the tetrahydrofolate leaving group. Furthermore, the β-DADF-bound structure provides a more optimal three-dimensional scaffold to improve the design of specific antineoplastic agents.

The advent of antifolate development as potential chemotherapeutic agents in the 1940s and 50s was due to the finding that children with leukemia had reduced levels of the essential vitamin folate (*1*). Folic acid and its cellular derivatives are utilized in many metabolic systems including the de novo purine and pyrimidine biosynthetic pathways, both of which are involved in cellular proliferation. The corelationship of cellular reproduction with folate depletion, via de novo syntheses, targets these pathways for the advancement of antifolates for cancer therapeutics. Specifically, the high proliferation rate of cancerous cells relative to normal cells, and their inability to rely solely on the salvage pathway for production of purines and pyrimidines, that are required for DNA synthesis, supports drug design efforts to inhibit both pathways (*2*). Therefore, design of an antifolate for inhibition of folate-dependent enzymes involved in de novo synthesis could result in a potential antineoplastic agent.

The de novo purine synthesis pathway converts phosphribosylpyrophosphate (PRPP)[1] to inosine monophosphate (IMP) in a 10-step reaction sequence in which two of the catalytic processes require a reduced folate cofactor, N_{10}-formyl-tetrahydrofolate (10-f-THF). Aminoimidazole-4-carboxamide ribonucleotide (AICAR) transformylase/inosine monophosphate cyclohydrolase (ATIC) (*3*) is one of the two de novo purine transformylases requiring 10-f-THF. ATIC is a bifunctional enzyme responsible for the final two catalytic steps of the pathway. AICAR transformylase (AICAR Tfase) catalyzes the penultimate step of de novo synthesis by transferring a formyl group from 10-f-THF to

---

[†] This work was supported by the National Institute of Health Grant PO1 CA63536 (I.A.W. and S.J.B.), and National Science Foundation and Skaggs predoctoral fellowships (D.W.W.). This is publication 15694-MB from The Scripps Research Institute.

[‡] The coordinates and structure factors have been deposited with the Protein Data Bank with ID entry 1O20.

* To whom correspondence should be addressed. E-mail: wilson@scripps.edu. Phone: 858.784.9706. Fax: 858.784.2980.

[§] The Scripps Research Institute.

[||] Present address: Agouron Pharmaceuticals, Inc., 10777 Science Center Drive, San Diego, CA 92121.

[⊥] Pennsylvania State University.

[@] Present address: 3-Dimensional Pharmaceuticals, Eagleview Corporate Center, 665 Stockton Drive, Suite 104, Exton, PA 19341.

[1] Abbreviations: PRPP, phosphribosylpyrophosphate; IMP, inosine monophosphate; 10-f-THF, N_{10}-formyl-tetrahydrofolate; AICAR, aminoimidazole-4-carboxamide ribonucleotide; ATIC, aminoimidazole-4-carboxamide ribonucleotide transformylase/inosine monophosphate cyclohydrolase; AICAR Tfase, AICAR transformylase; FAICAR, 5-formyl-AICAR; THF, tetrahydrofolate; IMPCH, IMP cyclohydrolase; MAI, multisubstrate adduct inhibitor; PALA, phosphoacetyl-L-aspartate; NCS, noncrystallographic symmetry; GAR, glycinamide ribonucleotide; GAR Tfase, GAR transformylase; β-TGDDF, β-thio-GAR-dideazafolate; TS, thymidylate synthase; FPGS, folylpoly-γ-glutamate synthetase; 10-f-TDAF, 10-formyl-5,8,10-trideazafolic acid; 10-f-DDF, 10-formyl-5,8-dideazafolate; DHFR, dihydrofolate reductase; RFC1, reduced folate carrier; iNOS, inducible nitric-oxide synthase; HIV, human immunodeficiency virus.

10.1021/bi030106h CCC: $25.00

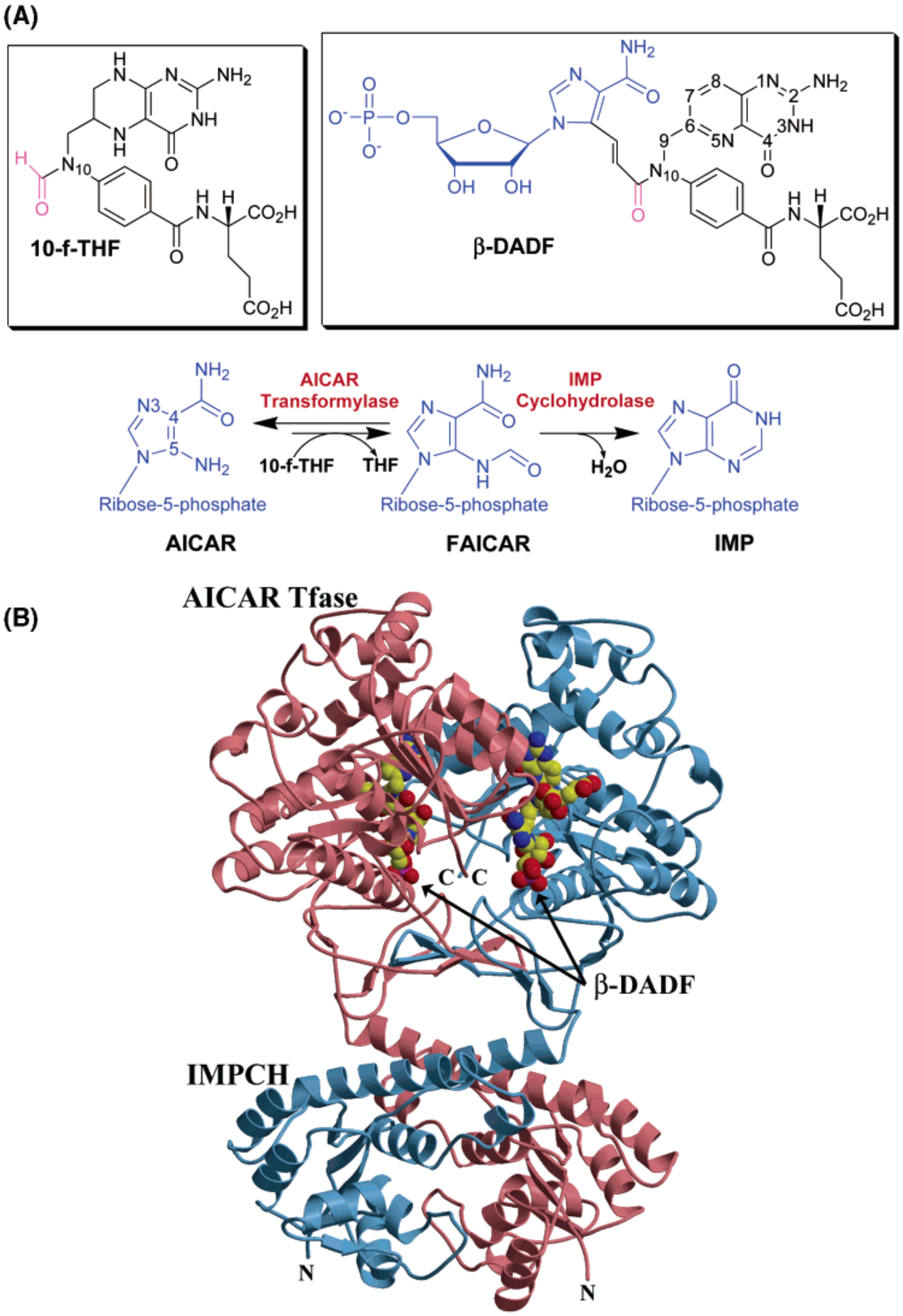

FIGURE 1: Reaction and crystal structure of ATIC. (A) Formyl transfer and IMP cyclohydrolase reactions catalyzed by ATIC, the structure of the folate cofactor (10-f-THF), and the multisubstrate adduct inhibitor β-DADF combining features of both substrate AICAR and 10-f-THF, are shown above in the black boxes. β-DADF is depicted with the AICAR moiety in blue, the 10-carbonyl equivalent to the 10-formyl group of the natural cofactor is in purple, and the folate portion is in black. (B) Overall view of the ATIC dimer. Subunit A is colored in teal, with subunit B colored in salmon. The two bound β-DADF molecules are depicted in a cpk representation (carbon-yellow, oxygen-red, nitrogen-blue and phosphate-purple). The N- and C- termini are labeled accordingly.

the substrate AICAR. The resulting products are the stable intermediate 5-formyl-AICAR (FAICAR) and the byproduct tetrahydrofolate (THF) (Figure 1A). FAICAR is subsequently involved in the cyclization reaction performed in the IMP cyclohydrolase (IMPCH) domain producing the end product of the pathway IMP.

Multisubstrate adduct inhibition (MAI) has been successful for designing potent inhibitors including phosphoacetyl-L-aspartate (PALA), specific for L-aspartate carbamoyl transferase, which was the first MAI to reach clinical trials (*4*−*6*). An MAI for ATIC was designed and synthesized by covalently linking the AICAR and folate moieties with a rigid trans double-bond via two methenyls (Figure 1A) (*7*). To ease synthesis of the MAI, an 8-deazafolate analogue was substituted for the reduced pterin ring of THF; this analogue has previously been used as an alternate cofactor for the formyl transfer reaction with a K_m of 102 μM (K_m of 10-f-THF is 68 μM) (*7*). However, the β-DADF MAI has an additional carbon atom within the linker between the AICAR and folate moieties that increases the distance between the substrate and cofactor by approximately 1.5 Å compared to the transition state. The β-DADF K_d and the IC_{50} are 20 and 125 nM, respectively, indicating that β-DADF is a potent inhibitor of AICAR Tfase (*7*). Unfortunately, the K_i could not be determined readily as β-DADF competes directly with both AICAR and 10-f-THF.

The crystal structure of avian ATIC in complex with β-DADF was determined primarily to identify the location of the folate binding pocket within the AICAR Tfase active site. The β-DADF-bound structure is significant for two additional reasons: (i) the location of the folate moiety corroborates the formyl transfer mechanism that we previously proposed from the substrate-bound ATIC complex (*8*); and (ii) this structural template can aid in future development of inhibitors with more optimal pharmacokinetic properties against the AICAR Tfase active site.

MATERIALS AND METHODS

Protein Expression and Purification. Avian ATIC was prepared as previously reported (*8*). Approximately 20 mg of pure homodimeric avian ATIC can be obtained from a 1 L preparation of *Escherichia coli* cells. β-DADF was added in a 10-fold molar excess to the avian ATIC protein (0.1−0.4 mg/mL), heated for 30 min in a 37 °C water bath to prevent precipitation, and incubated overnight at 4 °C. The samples were then concentrated to approximately 10 mg/mL using Millipore Ultrafree-15 filters (MWCO of 10 000 Da) and stored at 4 °C for crystallization experiments. The N-terminal His_6-tag was not removed via thrombin cleavage as the tagged ATIC crystallizes readily.

Crystallization and Data Collection. Protein crystals were grown at 22 °C by the sitting drop-vapor diffusion method by mixing equal volumes of avian ATIC (10 mg/mL) with a reservoir solution consisting of 13% (w/v) PEG 8000, 0.2 M imidazole, pH 7.0, and 5 mM DTT. Data were collected to 2.5 Å resolution on a single, flash-cooled crystal at −173 °C in a cryoprotectant consisting of well buffer and 20% MPD on beamline 9.1 at the Stanford Synchrotron Radiation Laboratory (SSRL) (Menlo Park, CA). Data were processed to 2.5 Å with the DENZO−SCALEPACK suite (*9*).

Structure Determination and Refinement. The molecular replacement solution was determined using the apo avian ATIC structure (*10*) (PDB entry 1G8M) as the search model in EPMR (*11*). EPMR places the search model randomly in the asymmetric unit and utilizes an evolutionary search algorithm to identify the most likely solutions. Following molecular replacement, the correlation coefficient and R_{cryst} were 68.7 and 36.0%, respectively. Further rigid body refinement against the maximum likelihood target (*12*) in CNS (*13*) yielded an R_{cryst} of 32.7% (R_{free} of 32.6%).

The initial electron density maps clearly identified β-DADF within both AICAR Tfase active sites. Model interpretation involved 17 cycles of rebuilding and refinement including simulated annealing, conjugate-gradient minimization, restrained individual temperature factors, and a bulk solvent correction. Due to the resolution limit of 2.5 Å, 2-fold noncrystallographic symmetry (NCS) was applied to the main-chain atoms of the monomers throughout refinement with a minimal NCS-restraint weight of 100. Water molecules were automatically positioned by CNS using a 3σ cutoff in F_o-F_c maps and manually inspected. The model was manually fitted to σ_A-weighted $3F_o-2F_c$ maps (*14*) with O (*15*). The final refined structure (Table 1) consists of all residues in each monomer, except 1−3 and the 20 additional N-terminal residues encompassing the His_6-tag and thrombin cleavage site.

Table 1: Data Processing and Refinement Statistics

Data Processing	
resolution range (Å) (outer shell)	50−2.50 (2.54−2.50)
unique reflections	39623 (1825)
completeness (%)	92.5 (85.8)
redundancy	2.1 (1.9)
R_{sym} (%)[a]	5.5 (42.4)
average $I/\sigma(I)$	14.0 (1.8)
Refinement	
resolution range (Å) (outer shell)	50.0−2.50 (2.52−2.50)
no. of reflections[b]	38094 (695)
R_{cryst} (%)[c]	21.7% (44.4%)
R_{free} (%)[c]	26.9% (46.5%)
protein atoms/waters	9022/378
CV[4] coordinate error (Å)	0.56
rmsd bonds (Å)/angles (°)	0.008/1.4
$\langle B \rangle$ all atoms/waters/ligands ($Å^2$)	43.2/43.8/56.6
Ramachandran Statistics (%)	
most favored	90.3
additional allowed	9.7
generously allowed	0.0
disallowed	0.0

[a] $R_{sym} = 100\Sigma_h\Sigma_i|I(h)_i - \langle I(h)\rangle|/\Sigma_h I(h)$ where $I(h)_i$ is the *i*th measurement of reflection *h* and $\langle I(h)\rangle$ is the average measurement value. [b] Reflections with $I > 0$ were used for refinement. [c] $R_{cryst} = \Sigma_h||F_o|-|F_c||/\Sigma_h|F_o|$, where F_o and F_c are the structure factor amplitudes from the data and the model, respectively. R_{free} is R_{cryst} with 8.7% test set structure factors. [d] Cross-validated (CV) coordinate errors from σ_A plots.

The model was analyzed with CNS (*13*), CCP4 (*16*), PROCHECK (*17*), and WHATCHECK (*18*). SC (*16*) and MS (*19*) programs were utilized to determine the S_c coefficients (*20*) and buried surface areas using 1.7 and 1.4 Å probes, respectively. Hydrogen bonds and van der Waals interactions were identified with CONTACSYM (*21*) with default parameters. R.m.s. deviation (rmsd) calculations on the β-DADF-bound, the previously determined AICAR/XMP-bound (PDB entry 1M9N) and apo avian (1G8M) ATIC structures were carried out with PROFIT (Martin, A. C. R., SciTech Software, Chico, CA). Superposition of monomer A of the β-DADF complex onto monomer B gave an rmsd of 0.52 Å for the main chain and 0.93 Å for all atoms, whereas the corresponding values were 0.71 and 1.12 Å for the IMPCH domain (residues 4−199) and 0.30 and 0.78 Å for the AICAR Tfase domain (residues 200−593). Figures 1B through 4A and 5 were created with Bobscript (*22*) and rendered with Raster3D (*23*). Figure 4B was created with PyMol (*24*). Coordinates and structure factors have been deposited without hold in the PDB (*25*), with accession entry 1OZ0.

RESULTS

Full-length avian ATIC (residues 1−593) was expressed in *Escherichia coli* and purified by gel filtration, as previously described (*8*, *10*). ATIC in the presence of a 10-fold molar excess of β-DADF readily crystallized overnight at room temperature in monoclinic space group $P2_1$ ($a = 54.41$ Å, $b = 108.10$ Å, $c = 102.36$ Å, and $\beta = 91.92°$). The

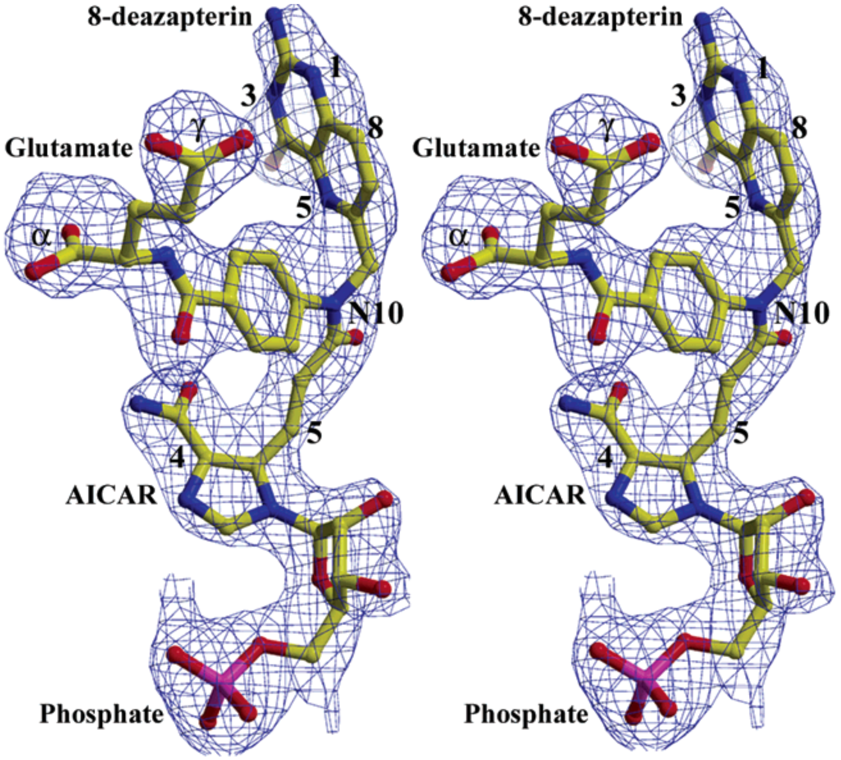

FIGURE 2: Structure of β-DADF. Stereoview of β-DADF bound to the AICAR Tfase active site with a F_o-F_c simulated-annealing omit map (blue) contoured at 2.5σ. β-DADF is represented in ball-and-stick representation with atoms colored according to Figure 1B.

structure was determined to 2.5 Å by molecular replacement (MR) using the apo avian ATIC (1G8M) as the search model (*10*). The final R_{cryst} and R_{free} values were 21.7 and 26.9%, respectively, with 90.3% of the residues in the most favored region of the Ramachandran plot (Table 1). The final refined model consists of residues 4−593 of both monomers, two β-DADF molecules in the AICAR Tfase active sites, two phosphate ions in the IMPCH active sites, two potassium ions, and 378 water molecules (Figure 1B).

Avian ATIC Topology. The ATIC monomer is composed of two functionally independent domains, IMPCH (residues 4−199) and AICAR Tfase (residues 200−593), that represent the two individual transformations catalyzed (Figure 1B). The IMPCH domain contains the common Rossmann mononucleotide binding fold within a parallel 5-stranded β-sheet (strand order 5−4−1−2−3) surrounded by three helices on one side of the sheet and seven on the other. However, the IMPCH domain does not contain any typical mononucleotide or phosphate binding motifs nor any GXXGXGK or GXGXXG (X represents any residue) fingerprints within its sequence. The AICAR Tfase domain can be further divided into three structural subdomains as previously described (*8*, *10*). Subdomains 2 (residues 200−374) and 4 (residues 375−593) are structurally homologous and have a primarily parallel five-stranded β-sheet with α-helices on both sides. Subdomain 3 (residues 469−532) is inserted within subdomain 4 and has a unique topology composed of four α-helices and two β-strands (*8*, *10*). In comparison to homodimeric proteins of similar molecular weight, the dimeric interface of ATIC has a large buried surface area of 4986 Å^2 (using a 1.4 Å probe) compared to the average of 3500 Å^2 (*10*) with a significant shape complementarity (S_c) (*20*) of 0.71 (using a 1.7 Å probe).

IMPCH Domain. The β-DADF-bound ATIC structure varies little from the two previously published avian ATIC structures (*8*, *10*), including the native enzyme (1G8M) which contained an endogenous bound nucleotide (rmsd for monomers A and B are 0.76 and 0.67 Å, respectively) and the AICAR/XMP-bound ATIC (1M9N) (rmsd for monomers A and B are 0.73 and 0.78 Å, respectively). As previously shown, significant side-chain and main-chain rearrangements occur upon binding XMP to the IMPCH active site (*8*, *10*). During model building and refinement, F_o-F_c maps revealed weak positive density located in the IMPCH active site of monomer B. A purine monophosphate moiety could be positioned into the density, but refinement did not decrease the *R* values and led to negative density in subsequent maps. Therefore, a bound phosphate was refined rather than XMP within both IMPCH active sites.

AICAR Tfase Domain. Unlike the IMPCH domain, very little rearrangements occur upon binding the MAI in the AICAR Tfase domain. The only significant change is in subdomain 3 (residues 469−532), where main-chain displacements of up to 3.0 Å rms deviations are found (residues 500−505), as well as increased *B* values (55 Å^2 for subdomain 3 versus 43 Å^2 for all protein atoms), these differences are likely due to differential crystal contacts, as suggested previously (*8*), and not ligand binding.

It was evident from the initial F_o-F_c maps that β-DADF was bound to both AICAR Tfase active sites of the dimer and could be easily positioned from superimposition of the AICAR/XMP-bound structure. The covalent link between the AICAR moiety and the folate portion was clearly identifiable, as well as the orientation of the folate moiety based on the 8-deazapterin and benzoyl ring densities (Figure 2). The trans double bond in the covalent linker has been

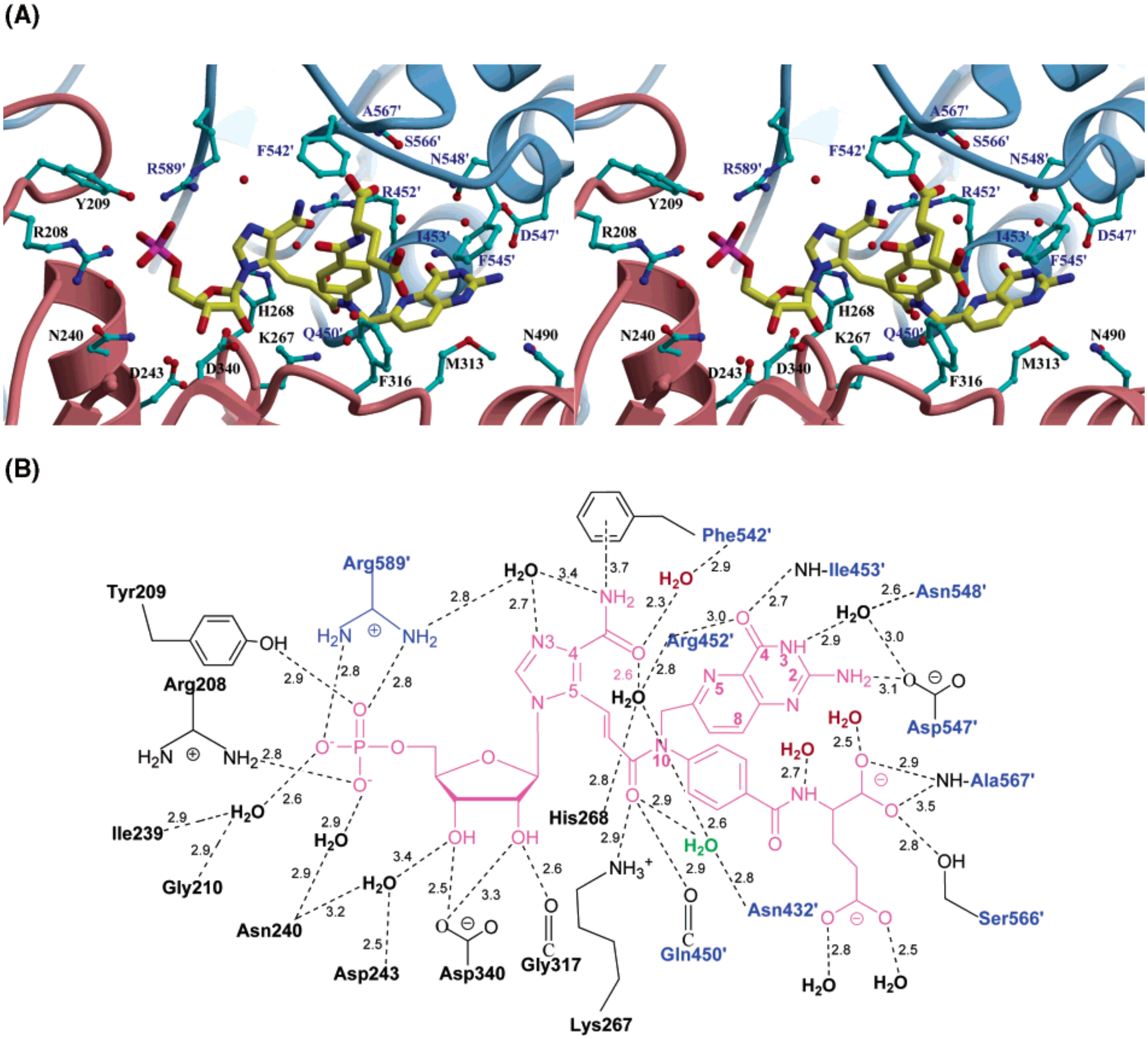

FIGURE 3: The AICAR Tfase active site. (A) Interactions among the residues that make up the AICAR binding site and β-DADF. β-DADF and active site residues are represented in ball-and-stick with β-DADF atoms color-coded as in Figure 1B. Carbon atoms of active site residues are colored cyan. Asn^{490} is not within hydrogen bonding distance, but could be a potential anchoring residue for the natural cofactor. (B) Schematic representation of the hydrogen bonding network and corresponding distances within the active site between β-DADF and AICAR Tfase. Interacting residues from the subunit opposite of the AICAR-bound monomer (black) are labeled in blue and β-DADF is colored pink. Water molecules that are found only in monomer A are labeled red and the water molecule specific to monomer B is labeled green. Side chains are depicted for only those residues that provide direct interactions to AICAR.

refined with a torsion angle of −173°, in the range of peptide torsion deviations.

Identification of the folate binding pocket further supports the dimeric requirement for activity (*8*, *26*). The AICAR and folate binding pockets are both located in an extensive cleft at the dimer interface between the two ATIC subunits. However, the majority of AICAR interactions occur with one subunit, while the primary folate interactions occur with opposing subunit (Figure 3A,B).

No significant differences in location, orientation, and conformation of β-DADF, or in the binding site side-chain conformations, were found between the two active sites. Close similarity in main chains of the two ATIC subunits was expected as NCS restraints were successfully applied; however, NCS was not applied to β-DADF or active site side chains. The location of several water molecules around β-DADF were not conserved (Figure 3B). The close superposition of AICAR in the AICAR/XMP-bound structure with the AICAR moiety of β-DADF suggests that the covalent link between the AICAR and folate portions of β-DADF does not unduly compromise binding of the AICAR component of the MAI within the active site (Figure 4A). Thus, given that the AICAR moiety is positioned similarly to the free AICAR substrate, the additional carbon in the covalent link between AICAR and folate could then potentially perturb binding of the folate moiety by up to approximately 2 Å.

Interactions with β-DADF AICAR Moiety. β-DADF is buried in a cleft within the AICAR Tfase active site with only approximately 23% (159 Å^2) of its surface area (700 Å^2) exposed to bulk solvent (Figure 4B). The individual buried surface area for the AICAR and folate moieties are 235 Å^2 (83%) and 354 Å^2 (65%), respectively (using a 1.4 Å probe). The AICAR in the AICAR-bound structure was 84% buried (238 Å^2) from solvent; therefore, the additional exposed surface in the MAI arises primarily from the folate portion of the inhibitor (*8*). The slight deviations in the orientation of the AICAR moiety from the AICAR/XMP-bound structure (Figures 3A,B and 4A) around the 4-car-

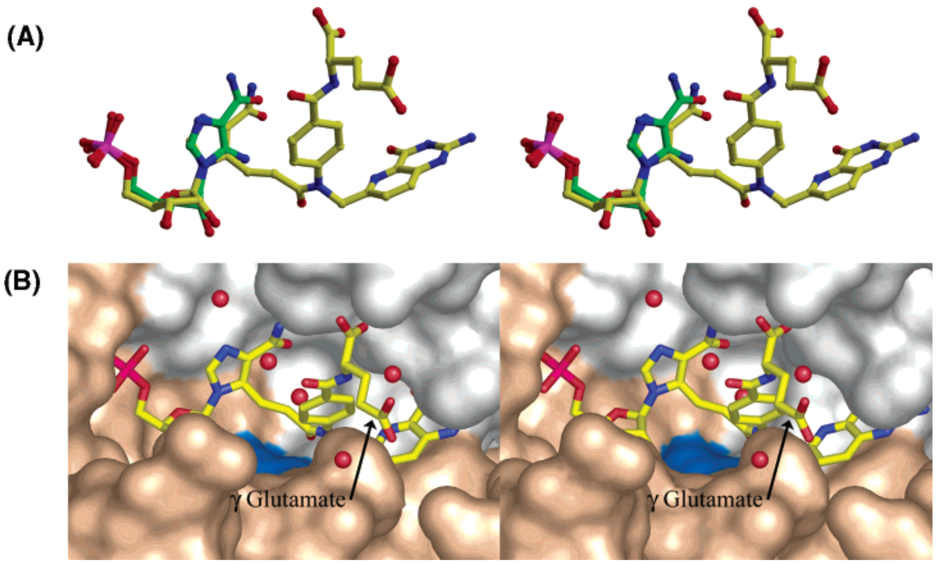

FIGURE 4: Superposition of AICAR and β-DADF and surface representation of AICAR Tfase active site. (A) Stereoview of β-DADF colored according to Figure 1B, superimposed on AICAR (carbon atoms colored green). Superposition of the two bound molecules reveals that the covalent linker to the folate moiety does not affect the AICAR position and orientation in β-DADF. (B) β-DADF bound within the AICAR Tfase binding site. The γ glutamate is labeled accordingly and β-DADF is shown in a stick representation colored as in Figure 1B. The solvent accessible surface of the AICAR-bound subunit is colored wheat and the folate-bound subunit is colored grayish white. The protruding tip of Lys^{267} is highlighted in teal.

boxamide likely reflects some slight accommodation due to the constrained covalent linkage to the folate moiety. The β-DADF phosphate is anchored via Arg^{208}, Tyr^{209}, and Arg$^{589'}$ (from the opposite subunit) (Figure 3B). Ordered water molecules are positioned near the phosphate through main-chain interactions provided by Gly^{210}, Ile^{239}, and Asn^{240}; this hydration shell is also observed in the AICAR/XMP-bound structure (*8*). The Asp^{340} side-chain and Gly^{317} main-chain interactions with the ribose ring hydroxyls appear to stabilize the sugar in a 3′-endo pucker conformation. The 4-carboxamide amino group maintains the π hydrogen bond interaction (3.7 Å) with the Phe$^{542'}$ aromatic ring of the opposite subunit, as previously observed (*8*). His^{268} cannot provide a hydrogen bond to the MAI inhibitor, because β-DADF has a carbon substituted for the 5-amino group (Figure 1A). Nevertheless, superposition with the AICAR-bound active site reveals that all side-chain conformations, including His^{268}, are conserved. His^{268} does, however, assist in positioning a water molecule, which also hydrogen bonds to the 4-carboxamide oxygen (Figure 3B), as in the AICAR/XMP structure.

Interactions with β-DADF Folate Moiety. The primary interactions of the AICAR Tfase active site with the folate portion of β-DADF are provided by the opposing subunit relative to that which primarily binds AICAR (Figure 3B). The 8-deazapterin ring is sandwiched between Phe$^{545'}$ of the folate-bound subunit and Met^{313} of the AICAR-bound subunit. Phe$^{545'}$ provides both a hydrophobic environment for the aromatic pterin ring, as well as a potential hydrogen bond acceptor for the 2-amino group as one of the amino hydrogens orients toward the center of the phenyl ring (Figure 3A). The main-chain amides of Arg$^{452'}$ and Ile$^{453'}$ donate hydrogen bonds to the 4-carbonyl of the 8-deazapterin ring (Figure 3B). Orientation of the 8-deazapterin ring may also be dictated by interaction of the exocyclic 4-carbonyl with the dipole at the N-terminus of an adjacent α-helix (residues 451−469). The exocyclic 2-amino group of the pterin ring interacts with the side chain of Asp$^{547'}$. The side chains of Asp$^{547'}$ and Asn$^{548'}$ also indirectly orient the pterin ring N3 nitrogen via bound water molecules (Figure 3B). The aromatic benzoyl ring is held in place via a perpendicular π-stacking interaction with Phe^{316}. The β-DADF α-glutamate interacts with the main-chain and side-chain of Ala$^{567'}$ and Ser$^{566'}$, respectively (Figure 3A), whereas the γ glutamate is not buried in the AICAR Tfase active site and makes hydrogen bonds only with surface water molecules (Figures 4B and 5). Further γ-polyglutamation (up to seven) of folates increases their cellular retention (*27*) through enhancement of the folate negative charge that inhibits reverse membrane transport. The increased affinity of polyglutamated folates and antifolates to their target proteins may also contribute to their retention and inhibitory properties through interaction with electropositive surfaces located near their active sites (*28*, *29*).

The 10-carbonyl of β-DADF (that mimics 10-formyl) has two interactions with the Lys^{267} amino group and the Gln$^{450'}$ main chain (Figure 3B). Lys^{267} provides the only direct hydrophilic interaction with the folate portion of β-DADF that is from the AICAR-bound subunit. The hydrogen bond between Lys^{267} and 10-formyl of the natural cofactor (2.9 Å) was previously predicted to be involved in the stabilization of the oxyanion transition state and in protonation of the N10 leaving group (*8*). A water molecule is also positioned within hydrogen bonding distance of the 10-formyl group via a side-chain interaction with Asn$^{432'}$, but is only observed in monomer B.

DISCUSSION

The crystal structure of avian ATIC in complex with the multisubstrate adduct inhibitor β-DADF (*7*) provides the first structural verification of the folate binding region of the AICAR Tfase active site and identifies the specific residues that not only anchor the folate, but are also likely to play a role in the formyl transfer reaction. The AICAR Tfase active site is situated at the dimer interface with a majority of interactions to AICAR being supplied by one subunit, while the folate interactions primarily occur with residues of the opposing monomer of the dimer (Figure 3A,B). Despite having the AICAR and folate moieties covalently tethered together in the MAI, the β-DADF-bound avian ATIC structure indicates that the AICAR moiety remains essentially in the same position, although slightly rotated, relative to that in the AICAR/XMP-bound structure (*8*) (Figure 4A). Further, in comparison to ATIC structures bound with folate-based inhibitors currently in refinement in our laboratory (Cheong et al., unpublished results), the location and orientation of the folate is not compromised greatly (but possibly up to 2 Å) due to the covalent attachment to the AICAR moiety. As the location and orientation of all of the key players in the ATIC formyl transfer reaction have now been elucidated, we can now suggest potential improvements in inhibitor design and provide further support for the anticipated role of Lys^{267} in the formyl transfer mechanism (*8*).

Consequences of Substitution of 8-Deazapterin for Reduced Folate Pterin. When designing a multisubstrate adduct inhibitor, the affinity of the inhibitor could potentially approach the product of the substrate K_m's. Therefore, with a K_m of 16.8 μM for AICAR (*30*) and 68 μM for 10-f-THF (*7*, *31*), the inhibition of β-DADF on AICAR transformylase could approximate a 1 nM K_d. It was possible to approach picomolar inhibition for glycinamide ribonucleotide (GAR) transformylase (GAR Tfase) MAIs BW1476U89 (*32*, *33*) and β-thio-GAR-dideazafolate (β-TGDDF) (*34*, *35*) as their substrate GAR and folate cofactor K_m's are approximately 10-fold lower than the comparable values for ATIC. However, the anticipated gain in binding an MAI may not be realized due to enthalpically-diminished binding capabilities (*36*). The more conformationally restricted a polyvalent molecule becomes, the less likely that the binding would approach the maximal K_d as even the smallest discrepancies in binding, in comparison to natural ligands, decrease the enthalpy of interaction (*36*). Nevertheless, redesign of β-DADF (K_d of 20 nM) could potentially improve its inhibitory properties of the folate by substitution of the 8-deazapterin ring for a reduced ring, removal of the rigid trans double bond linker, replacement of the 5-menthyl of AICAR with a nitrogen and the deletion of the extra carbon atom within the link between the AICAR and folate moieties. These modifications could potentially decrease any strain or misorientation of the covalently-linked moieties relative to their untethered states and also enhance binding with substitution by the natural folate cofactor moiety.

Some potential interactions with the natural cofactor are probably not possible with the MAI due to the increased rigidity of β-DADF from the aromatic substitution of the 8-deazapterin for tetrahydrofolate and the restrictions posed by the rigid covalent double-bond linker to AICAR (Figure 1A); the lack of reduced nitrogen atoms at positions 5 and 8 remove potential hydrogen bond donors, that could interact with potential hydrogen bond acceptors, such as Ser$^{451'}$ and Asn^{490} (Figure 3A). Ser$^{451'}$ could potentially interact with the reduced N5 position of the pterin; however, steric clashes occur due to the aromaticity of deazapterin such that the Ser$^{451'}$ hydroxyl side chain points away from the active site. Similarly, the side chain of Asn^{490} could serve as both a hydrogen bond donor and acceptor for the pterin ring's reduced N8 and acceptor nitrogen at position 1. The Asn^{490} carboxamide is currently positioned approximately 5.5 Å from the donor/acceptor array of the pterin ring and most likely cannot interact due to restrictions placed in the location and orientation of the 8-deazapterin by covalent attachment to AICAR (Figure 3A). Some of these features could also account for the differences in K_m's of 10-f-THF and 10-formyl-8-deazafolate (68 and 102 μM, respectively) (*7*).

Effects of Carbon Substitution for the 5-Amino in β-DADF. The 5-amino group which performs the nucleophilic attack on the 10-f-THF was replaced by a methenyl group in β-DADF, as a consequence of the difficulty in finding a suitable electrophile that would react with the amine to achieve covalent linkage of the folate and AICAR moieties (*7*). Replacement of the 5-amino group of AICAR also likely contributes to the decrease in optimal binding capacity of this MAI and to some slight orientational differences in the AICAR moiety with respect to AICAR in the AICAR/XMP-bound structure (Figure 4A). The loss of a critical interaction with His^{268}, which has been proposed to be a key player in the formyl transfer mechanism (*8*), is a consequence of removing the 5-amino group. Overall, the imidazole ring of the AICAR moiety is torsioned approximately 25° from its orientation in the AICAR-bound structure (Figure 4A), most likely due mainly to the strain encountered with the covalent link to the folate. The 4-carboxamide is slightly tilted to alleviate steric clashes with the AICAR methenyl substitution. In the AICAR-bound structure, the 5-amino group and the 4-carboxamide oxygen were 2.9 Å apart, which increases here to 3.4 Å for the 4-carboxamide oxygen to the β-DADF carbon linker. Despite these differences, the 4-carboxamide amino group maintains a π hydrogen bond interaction (*37*) with Phe$^{542'}$ (*8*).

Location, Orientation, and Interactions with the Carbonyl of β-DADF. The covalent linker contains an additional carbon in comparison to the natural transition state of the formyl transfer reaction. Surprisingly, the covalent trans double-bond linker in β-DADF appears only to cause some slight orientation and positional variations in the AICAR and folate moieties. Several residues within the active site have been previously proposed to play key roles in the catalytic process (*8*). His^{268} was postulated to abstract a proton from the 5-amino group of AICAR simultaneous with nucleophilic attack on 10-f-THF, while Lys^{267} is likely to stabilize the oxyanion transition state and subsequent protonation of the N10 THF leaving group (*8*). In this MAI structure, Lys^{267} has extremely well-defined density with its side-chain amino group pointing toward the β-DADF N10 carbonyl oxygen at a distance of 2.9 Å, consistent with its proposed role.

The distance between the AICAR 5-amino and the formyl group carbon of the cofactor eventually needs to approach 1.4−1.5 Å to form a covalent C−N bond in the formyl transfer reaction. More importantly, the two atoms need to be oriented appropriately to facilitate nucleophilic attack on the formyl group by the 5-amino of AICAR. Due to the linker region, the β-DADF compound has these equivalent atoms fixed at a distance of 2.9 Å, which precludes this region of being an optimal mimic of the transition state. The Lys^{267} side chain is 3.7 Å from N10 of β-DADF; however, this value may decrease in unconstrained folate analogues, when the natural cofactor is bound, or during the catalytic cycle. Lys^{267} is approximately 92% buried within the active site in the absence of β-DADF (using a 1.4 Å probe) and completely buried when β-DADF is present (Figure 4B). The buried Lys^{267} side chain is in a semi-hydrophobic environment suggests that its pK_a would be perturbed so as to favor a population of uncharged conformers in the resting state of the protein. As the formyl transfer equilibrium lies heavily toward the starting substrates (*38*, *39*), Lys^{267} is appropriately poised to abstract a proton from N10 in the reverse formyl transfer reaction. In the forward formyl transfer from 10-f-THF to AICAR, Lys^{267} may facilitate rapid proton shuffling and become transiently protonated in the transition state to stabilize the developing oxyanion at the formyl group and subsequent protonation of the N10.

Although Lys^{267} donates a hydrogen bond to the carbonyl β-DADF, a potential negative interaction arises from the proximity of the main-chain carbonyl of Gln$^{450'}$ (2.9 Å) to the MAI carbonyl oxygen. The location of Gln$^{450'}$ could serve two potential roles. The Gln$^{450'}$ main-chain carbonyl could assist in orienting the Lys^{267} side chain toward the formyl oxygen, being only 3.3 Å apart, and/or destabilize the oxyanion transition state. As the Lys^{267} side chain is not conformationally restricted in the AICAR Tfase active site (*8*), the interaction across the dimer interface with Gln$^{450'}$ could precisely position the Lys^{267} side chain for optimal interaction with the 10-f-THF. A second possibility is that the unfavorable steric clashes between the lone pairs of electrons from the carbonyl oxygen of β-DADF and the Gln$^{450'}$ main-chain carbonyl could intentionally exploit this negative interaction in the formyl transfer reaction. The location of the carbonyl of Gln$^{450'}$ and the position of the 5-amino group of AICAR oppose each other with the formyl group and Lys^{267} located between (Figure 3A). Development of repulsive interactions, initially between the 10-formyl oxygen and then the negatively-charged 10-formyl oxygen of the transition state analogue with the Gln$^{450'}$ main chain, could push the formyl group toward the 5-amino of AICAR to promote covalent bond formation.

Polyglutamated Tail. Antifolate binding studies against ATIC have shown that polyglutamation increases inhibition (*40*). Studies on the antifolate LY231514 have shown that, in its polyglutamated form, it is one of the most potent folate-based inhibitors against thymidylate synthase (TS) (*41*). Its inhibition abilities have also been tested on ATIC. The mono-, tri-, and pentaglutamated versions of LY231514 exhibited a 7-fold increase in K_i from mono- to triglutamated forms and an additional 2-fold increase from tri- to pentaglutamated forms (*40*). Folates and antifolates that contain a glutamate residue are converted within mammalian cells to a polyglutamated form through a γ peptide link which is added via folylpoly-γ-glutamate synthetase (FPGS). Each increase in the overall net charge improves cellular retention of the polyglutamated folate (*27*). The polyglutamation also results in greater inhibition of ATIC. However, the γ tail of the monoglutamate is the only portion of the molecule not buried by the protein (Figures 4B and 5); additional γ glutamate residues can easily be accommodated without disturbing the positioning of the cofactor moiety. Electrostatic surface potential calculations clearly show that the ATIC surface surrounding the glutamate is highly electropositive and complimentary to the addition of negatively charged glutamates, that thereby increase folate binding (Figure 5).

Comparison to MAI-Bound GAR Tfase Structures. ATIC and GAR Tfase perform similar formyl transfer reactions incorporating the same 10-f-THF cofactor despite the two enzymes having no significant sequence or structural homology. In comparison to the various structures of *E. coli* GAR Tfase in complex with antifolates BW1476U89 ($K_i \sim 100$ pM) (PDB entry 1GAR) (*33*), β-TGDDF ($K_d \sim 250$ pM) (*34*, *35*) and 10-formyl-5,8,10-trideazafolic acid (10-f-TDAF, $K_i = 260$ nM) (PDB entry 1C3E) (*42*), as well as the epoxide-derived MAI of β-GAR and 10-bromo-10-bromomethyl-5,8,10-trideazafolic acid ($K_i = 20\ \mu$M) (PDB entry 1JKX) (*43*), substantial differences are observed in the ways in which these related folates interact within the different active sites, and whether conformational changes in the protein accompany ligand binding. Unlike the epoxide-derived MAI which mimics the transition state, BW1476U89 was designed to incorporate only the structural features of GAR and 10-f-THF that were thought to contribute significantly to binding in the GAR Tfase active site (*32*, *33*) and were then connected via a flexible linker. In general, both AICAR Tfase and GAR Tfase folate-binding pockets sandwich the pterin ring between hydrophobic residues from both above and below, while hydrogen bonds interact with the plane of the heterocyclic ring further anchoring the inhibitor. In AICAR Tfase, the pterin ring is sandwiched between Phe$^{545'}$ and Met^{313}; however, the equivalent ring in GAR Tfase is enclosed in a deep cavity with five hydrophobic side chain interactions below (residues 85, 92, 96, 97, and 139) and a loop (residues 141−145) above the ring, respectively (*33*, *42*). All of the polar atoms within the cofactor pterin ring make hydrophilic interactions primarily with main-chain atoms in GAR Tfase (*33*, *42*, *43*), while a more limited number of hydrogen bonds are formed in AICAR Tfase with 8-deazapterin via the Arg$^{452'}$ and Ile$^{453'}$ main chain and Asp$^{547'}$ side chain. The benzoyl ring in β-DADF is held tightly in place by the perpendicular π stacking provided by Phe^{316} of ATIC, while the equivalent interactions in GAR Tfase antifolates are primarily weak hydrophobic interactions. The orientation of the benzoyl ring in GAR Tfase is defined by amide group hydrogen bonding with Met^{89} main-chain carbonyl (*33*, *43*). For both avian ATIC and human GAR Tfase, the α glutamate portions of the folates are anchored via protein hydrogen bonds, with

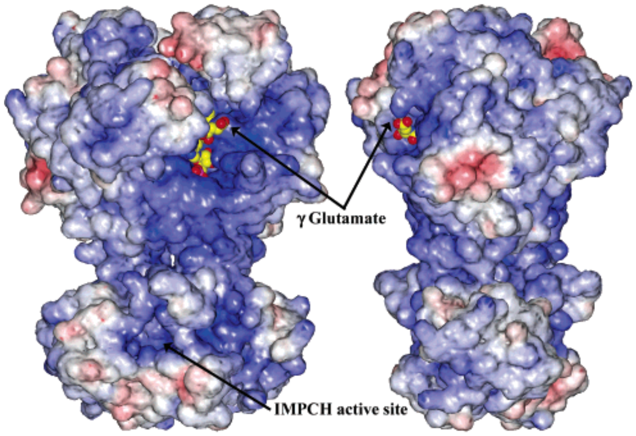

FIGURE 5: Electrostatic surface representation of ATIC. The electrostatic potential of the surface surrounding the AICAR Tfase active site. There is a 90° rotation between the two views of the complete ATIC. β-DADF is represented in cpk and is colored according to Figure 1B. Positive potential $\leq$10 mV) is blue, neutral potential (0 mV) is white and negative potential (≤ -10 mV) is red.

the γ glutamate positioned out of the active site. Carbonyls of the BW1476U89 (*33*) and epoxide-derived MAI (*43*) inhibitors that equate to the 10-formyl group of the natural cofactor interact with the side chains of His^{108} and Asn^{106} in GAR Tfase active site, both of which, and along with Asp^{144}, have been shown by mutational analysis to be required for catalysis (*44*). The interactions with the equivalent carbonyl of β-DADF are provided by the side chain of Lys^{267} and main chain of Gln$^{450'}$ in ATIC.

One of the major differences between the folate binding pockets of GAR Tfase and AICAR Tfase is the large conformational change in the “folate-dependent” loop (residues 141−145) in GAR Tfase which sequesters the folate from bulk solvent (*33*, *42*−*44*). No conformational changes appear to accompany binding of β-DADF in the active site of AICAR Tfase. The “folate-dependent” loop of GAR Tfase serves two purposes which include encasing the pterin ring of folate and bringing the catalytic Asp^{144} into proximity and appropriate orientation to aid in the formyl transfer (*33*, *44*). GAR Tfase has a higher affinity for folate over ATIC when in the “closed” loop conformation, thereby compensating for the entropic disadvantage of having a conformational rearrangement. This is reflected in respective K_m’s for 5,10-methenyl-tetrahydrofolate (K_m of 8.9 μM) (*31*) and 10-formyl-5,8-dideazafolate (10-f-DDF) (K_m of 12.3μM) (*45*) for GAR Tfase versus 10-f-THF (K_m of 68 μM) (*31*) and 10-formyl-8-deazafolate (K_m of 102 μM) (*7*) for ATIC. The BW1476U89 (*33*) and epoxide-derived MAI (*43*) GAR Tfase structures depict the “folate-dependent” loop in both a “closed” and “open” conformation, respectively. Buried surface area comparisons for the folate moieties of the epoxide-derived MAI and BW1476U89 in the GAR Tfase active site with β-DADF in the AICAR Tfase active site reveal that GAR Tfase sequesters folate in both the “open” (70% buried) and “closed” (83% buried) conformations to a greater extent than in ATIC (65% buried) (using 1.4 Å probe). The reversibility of the formyl transfer reaction might be a consequence of the accessibility of the AICAR Tfase active site.

Comparison of GAR Tfase, TS (PDB entry 1DHF) (*46*) and dihydrofolate reductase (DHFR) (PDB entry 2TDD) (*47*) shows that ATIC binds the trans folate conformation previously unique to GAR Tfase (*33*). In TS and DHFR, these enzymes bind folate with a g^+ conformation defined by the angle between atoms N5/C6/C9/N10 (~50° and 69°) (*33*, *47*, *48*). GAR Tfase orients the folate in a trans conformation with angles ranging from 166° to 174° (*33*). Therefore, the trans conformation may be important in the formyl transfer mechanism as both enzymes, despite having no structural homology, orient the folate similarly. The trans conformation of folate for both GAR Tfase and AICAR Tfase aligns the formyl group with the key catalytic residues for both enzymes. Superposition of the pterin rings of folates with the g^+ conformation into the active site of AICAR Tfase depicts the 10-formyl oxygen flipped “up” away from Lys^{267}.

Improvement of Inhibitor. The inhibitory properties of a potent MAI could ideally approximate the combined K_m’s for both the substrate and cofactor. β-DADF is the first such MAI-based inhibitor designed specifically for the AICAR Tfase domain (*7*) and improvements can now be suggested based on the current crystal structure and previously measured K_i’s for several folate-based inhibitors (*40*, *49*−*53*). Inhibitor design has primarily focused on manipulating the folate scaffold, as folates can be chaperoned through the cellular membrane via the reduced folate carrier (RFC1) and the folate receptor (*27*). Derivatives of the AICAR substrate have not been pursued due to their inability to be transported as a result of the negatively charged monophosphate group. Several key components of β-DADF can be preserved or substituted in the specific tailoring of antifolates for the AICAR Tfase active site as outlined above.

ATIC is unique among the folate-dependent proteins in that the binding pocket is located at the dimer interface and is composed of residues from both subunits. The dimeric assembly is required for AICAR Tfase activity (*26*). Thus, specific antifolate development against ATIC could focus on synthesis of allosteric dimerization inhibitors. Several small molecule dimerization inhibitors have been successfully developed for other proteins, including inducible nitric-oxide synthase (iNOS) (*54*, *55*), human immunodeficiency virus (HIV) reverse transcriptase (*56*) and HIV protease (*57*).

In designing a second generation MAI, several improvements could be incorporated to increase inhibition. The trans double carbon bond connecting the AICAR and folate moieties sterically hinders the folate of β-DADF from optimally binding in its respective pocket. A single bond would provide for more flexibility while maintaining the covalent attachment. Design of an MAI with a nitrogen atom in the 5-amino position would stabilize the positive interactions from both the 4-carboxamide oxygen and His^{268}.

In designing an effective inhibitor, one also has to consider how the compound will gain entry into the cell. The phosphate group of β-DADF provides a key anchor for ATIC binding; however, the phosphate inhibits cell entry as a result of its negative charge. Phosphate removal would most likely result in a greatly reduced K_i as illustrated by the 7000-fold reduction in affinity of the GAR Tfase inhibitor β-TGDDF (*58*). The phosphate group could be substituted for another functional group that could maintain hydrogen bonding with the protein. Alternatively, the antifolate could be designed such that once transported across the plasma membrane, it would react with substrate AICAR to form an enzyme-assembled MAI. This approach was successful for the 10-bromo-10-bromomethyl-5,8,10-trideazafolic acid inhibitor of GAR Tfase where it reacted with substrate GAR to form an enzyme-assembled, irreversible epoxide-derived MAI (*43*). The task of finding a suitable antifolate electrophile that would react with the nonnucleophilic 5-amino group of AICAR is the most challenging aspect of the design.

CONCLUSION

The β-DADF-bound structure of the AICAR Tfase active site has provided the first structural identification of the folate binding pocket, elaborated on the proposed role of Lys^{267} in catalysis (*8*), and has suggested several improvements that can be made in specifically tailoring an inhibitor to ATIC. The active site of the AICAR Tfase domain is situated at the dimer interface with the individual binding pockets for folate and AICAR primarily being located in opposing monomers. One of the critical “crossover” interactions is with Lys^{267} of the AICAR-bound subunit, as it interacts with the 10-carbonyl of β-DADF. This interaction was predicted to occur based on our previous AICAR/XMP-bound structure.

Lys^{267} becomes completely buried upon folate binding suggesting its $\mathrm{p}K_\mathrm{a}$ could be sufficiently perturbed to act as a proton shuttle during the formyl transfer reaction. Exploiting other proximal active site residues that are not utilized in binding the conformationally restricted β-DADF could provide additional interactions to improve the efficacy of second generation of inhibitors. A high-resolution crystal structure of ATIC in complex with the naturally occurring 10-f-THF would also greatly facilitate elucidation of other potential favorable interactions in the folate binding pocket and hence, how to improve MAI and folate-based inhibitor design.

ACKNOWLEDGMENT

We thank T. Horton for excellent technical support in protein expression and purification, A. Heine and X. Dai for data collection and processing, D. Boger and R. Stanfield for helpful suggestions and discussion, M. Elsliger for computational assistance, and the staff of SSRL beamline 9.1.

REFERENCES

1. Farber, S., Diamond, L. K., Mercer, R. D., Sylvester, R. F., and Wolff, J. A. (1948) *N. Engl. J. Med. 238*, 787−793.
2. Jackson, R. C., and Harkrader, R. J. (1981) in *Nucleosides and Cancer Treatment* (Tattersall, M. H. N., and Fox, R. M., Eds.) pp 18−31, Academic Press, Sydney.
3. Baldwin, S. W., Tse, A., Gossett, L. S., Taylor, E. C., Rosowsky, A., Shih, C., and Moran, R. G. (1991) *Biochemistry 30*, 1997−2006.
4. Collins, K. D., and Stark, G. R. (1971) *J. Biol. Chem. 246*, 6599−6605.
5. Muss, H. B., Slavik, M., Bundy, B., Stehman, F. B., and Creasman, W. T. (1984) *Am. J. Clin. Oncol. 7*, 257−260.
6. Broom, A. D. (1989) *J. Med. Chem. 32*, 2−7.
7. Wall, M., Shim, J. H., and Benkovic, S. J. (1999) *J. Med. Chem. 42*, 3421−3424.
8. Wolan, D. W., Greasley, S. E., Beardsley, G. P., and Wilson, I. A. (2002) *Biochemistry 41*, 15505−15513.
9. Otwinowski, Z., and Minor, W. (1997) *Methods Enzymol. 276*, 307−326.
10. Greasley, S. E., Horton, P., Ramcharan, J., Beardsley, G. P., Benkovic, S. J., and Wilson, I. A. (2001) *Nat. Struct. Biol. 8*, 402−406.
11. Kissinger, C. R., Gehlhaar, D. K., and Fogel, D. B. (1999) *Acta Crystallogr. D55*, 484−491.
12. Pannu, N. S., and Read, R. J. (1996) *Acta Crystallogr. A52*, 659−668.
13. Brünger, A. T., Adams, P. D., Clore, G. M., DeLano, W. L., P., G., Grosse-Kunstleve, R. W., Jiang, J.-S., Kuszewski, J., Nilges, N., Pannu, N. S., Read, R. J., Rice, L. M., Simonson, T., and Warren, G. L. (1998) *Acta Crystallogr. D54*, 905−921.
14. Read, R. J. (1986) *Acta Crystallogr. A42*, 140−149.
15. Jones, T. A., Cowan, S., Zou, J. Y., and Kjeldgaard, M. (1991) *Acta Crystallogr. A47*, 110−119.
16. CCP4. (1994) *Acta Crystallogr. D50*, 760−763.
17. Laskowski, R. A., MacArthur, M. W., Moss, D. S., and Thornton, J. M. (1993) *J. Appl. Crystallogr. 26*, 283−291.
18. Hooft, R. W., Vriend, G., Sander, C., and Abola, E. E. (1996) *Nature 381*, 272.
19. Connolly, M. L. (1983) *Science 221*, 709−713.
20. Lawrence, M. C., and Colman, P. M. (1993) *J. Mol. Biol. 234*, 946−950.
21. Sheriff, S., Hendrickson, W. A., and Smith, J. L. (1987) *J. Mol. Biol. 197*, 273−296.
22. Esnouf, R. M. (1997) *J. Mol. Graphics 15*, 132−134.
23. Merritt, E. A., and Murphy, M. E. P. (1994) *Acta Crystallogr. D50*, 869−873.
24. DeLano, W. L. (2002), *The PyMOL Molecular Graphics System*, DeLano Scientific.
25. Berman, H. M., Westbrook, J., Feng, Z., Gilliland, G., Bhat, T. N., Weissig, H., Shindyalov, I. N., and Bourne, P. E. (2000) *Nucleic Acids Res. 28*, 235−242.
26. Vergis, J. M., Bulock, K. G., Fleming, K. G., and Beardsley, G. P. (2001) *J. Biol. Chem. 276*, 7727−7733.
27. Calvert, H. (1999) *Semin. Oncol. 26*, 3−10.
28. Allegra, C. J., Drake, J. C., Jolivet, J., and Chabner, B. A. (1985) *Proc. Natl. Acad. Sci. U.S.A. 82*, 4881−4885.
29. Baggott, J. E., Vaughn, W. H., and Hudson, B. B. (1986) *Biochem. J. 236*, 193−200.
30. Rayl, E. A., Moroson, B. A., and Beardsley, G. P. (1996) *J. Biol. Chem. 271*, 2225−2233.
31. Smith, G. K., Mueller, W. T., Benkovic, P. A., and Benkovic, S. J. (1981) *Biochemistry 20*, 1241−1245.
32. Bigham, E. C., Hodson, S. J., Mallory, W. R., Wilson, D., Duch, D. S., Smith, G. K., and Ferone, R. (1992) *J. Med. Chem. 35*, 1399−1410.
33. Klein, C., Chen, P., Arevalo, J. H., Stura, E. A., Marolewski, A., Warren, M. S., Benkovic, S. J., and Wilson, I. A. (1995) *J. Mol. Biol. 249*, 153−175.
34. Inglese, J., Blatchly, R. A., and Benkovic, S. J. (1989) *J. Med. Chem. 32*, 937−940.
35. Inglese, J., and Benkovic, S. J. (1991) *Tetrahedron 47*, 2351−2364.
36. Mammen, M., Choi, S., and Whitesides, G. M. (1998) *Angew. Chem., Int. Ed. 37*, 2754−2794.
37. Levitt, M., and Perutz, M. F. (1988) *J. Mol. Biol. 201*, 751−754.
38. Wall, M., Shim, J. H., and Benkovic, S. J. (2000) *Biochemistry 39*, 11303−11311.
39. Bulock, K. G., Beardsley, G. P., and Anderson, K. S. (2002) *J. Biol. Chem. 277*, 22168−22174.
40. Shih, C., Chen, V. J., Gossett, L. S., Gates, S. B., MacKellar, W. C., Habeck, L. L., Shackelford, K. A., Mendelsohn, L. G., Soose, D. J., Patel, V. F., Andis, S. L., Bewley, J. R., Rayl, E. A., Moroson, B. A., Beardsley, G. P., Kohler, W., Ratnam, M., and Schultz, R. M. (1997) *Cancer Res. 57*, 1116−1123.
41. Taylor, E. C., Kuhnt, D., Shih, C., Rinzel, S. M., Grindey, G. B., Barredo, J., Jannatipour, M., and Moran, R. G. (1992) *J. Med. Chem. 35*, 4450−4454.
42. Greasley, S. E., Yamashita, M. M., Cai, H., Benkovic, S. J., Boger, D. L., and Wilson, I. A. (1999) *Biochemistry 38*, 16783−16793.
43. Greasley, S. E., Marsilje, T. H., Cai, H., Baker, S., Benkovic, S. J., Boger, D. L., and Wilson, I. A. (2001) *Biochemistry 40*, 13538−13547.
44. Su, Y., Yamashita, M. M., Greasley, S. E., Mullen, C. A., Jennings, P. A., Warren, M. S., Benkovic, S. J., and Wilson, I. A. (1998) *J. Mol. Biol. 281*, 485−499.
45. Shim, J. H., and Benkovic, S. J. (1998) *Biochemistry 37*, 8776−8782.
46. Davies, J. F. D., Delcamp, T. J., Prendergast, N. J., Ashford, V. A., Freisheim, J. H., and Kraut, J. (1990) *Biochemistry 29*, 9467−9479.
47. Perry, K. M., Carreras, C. W., Chang, L. C., Santi, D. V., and Stroud, R. M. (1993) *Biochemistry 32*, 7116−7125.
48. Davies, J. D., Wilson, D. H., Hermel, E., Lindahl, K. F., Butcher, G. W., and Wilson, D. B. (1991) *J. Exp. Med. 173*, 823−832.
49. Boger, D. L., Haynes, N. E., Kitos, P. A., Warren, M. S., Ramcharan, J., Marolewski, A. E., and Benkovic, S. J. (1997) *Bioorg. Med. Chem. 5*, 1817−1830.
50. Boger, D. L., Haynes, N. E., Warren, M. S., Gooljarsingh, L. T., Ramcharan, J., Kitos, P. A., and Benkovic, S. J. (1997) *Bioorg. Med. Chem. 5*, 1831−1838.
51. Boger, D. L., Haynes, N. E., Warren, M. S., Ramcharan, J., Kitos, P. A., and Benkovic, S. J. (1997) *Bioorg. Med. Chem. 5*, 1853−1857.
52. Boger, D. L., Haynes, N. E., Warren, M. S., Ramcharan, J., Kitos, P. A., and Benkovic, S. J. (1997) *Bioorg. Med. Chem. 5*, 1839−1846.
53. Boger, D. L., Haynes, N. E., Warren, M. S., Ramcharan, J., Marolewski, A. E., Kitos, P. A., and Benkovic, S. J. (1997) *Bioorg. Med. Chem. 5*, 1847−1852.
54. McMillan, K., Adler, M., Auld, D. S., Baldwin, J. J., Blasko, E., Browne, L. J., Chelsky, D., Davey, D., Dolle, R. E., Eagen, K. A., Erickson, S., Feldman, R. I., Glaser, C. B., Mallari, C., Morrissey, M. M., Ohlmeyer, M. H., Pan, G., Parkinson, J. F., Phillips, G. B., Polokoff, M. A., Sigal, N. H., Vergona, R., Whitlow, M., Young, T. A., and Devlin, J. J. (2000) *Proc. Natl. Acad. Sci. U.S.A. 97*, 1506−1511.

55. Blasko, E., Glaser, C. B., Devlin, J. J., Xia, W., Feldman, R. I., Polokoff, M. A., Phillips, G. B., Whitlow, M., Auld, D. S., McMillan, K., Ghosh, S., Stuehr, D. J., and Parkinson, J. F. (2002) *J. Biol. Chem. 277*, 295−302.

56. Sluis-Cremer, N., Arion, D., and Parniak, M. A. (2002) *Mol. Pharm. 62*, 398−405.

57. Shultz, M. D., Bowman, M. J., Ham, Y. W., Zhao, X., Tora, G., and Chmielewski, J. (2000) *Angew. Chem., Int. Ed. 39*, 2710−2713.

58. Inglese, J., Johnson, D. L., Shiau, A., Smith, J. M., and Benkovic, S. J. (1990) *Biochemistry 29*, 1436−1443.

BI030106H